Nonlinear dynamic simulation and parametric analysis of a rotor-AMB-TDB system experiencing strong base shock excitations

Abstract:
The introduction of active magnetic bearings (AMBs) has enabled turbomachinery to increase power density, controllability, and general resilience to external disturbances. However, because of the limited load capacity of AMBs, the base shock condition that "on-board" machines often encounter may result in contact between the rotor and the touchdown bearings (TDBs), which can seriously damage the machine. A challenge in AMB applications is to alleviate this problem. This study presents a dynamic analysis of a rotor-AMB-TDB system under strong base shocks while the AMBs are operating. Detailed TDB and contact models are presented using Hertzian contact theory. A PD controller was then designed considering system saturation and friction, based on the Coulomb model and the effect of lubrication. The dynamic equations were solved for the dynamic trajectory and FFT spectra, STFT spectra, Poincaré maps and bifurcation diagrams were used for the parametric analysis. The results show that the rotor had three motion modes. System parameters, including unbalance eccentricity, magnetic gap clearance and equivalent stiffness and damping ratio, may lead to complex nonlinear dynamic behavior including periodic, KT-periodic, and quasi-periodic responses and jump phenomenon. Suitable designs that consider these parameters may avoid undesirable rotor dynamic behavior. This study reveals the mechanism for nonlinear response, providing a method for its prediction, and core controller parameter designs for rotor re-levitation.

1. Introduction

Active Magnetic bearings (AMBs) have many advantages, such as non-contact operation without lubrication or sealing, low energy consumption and maintenance costs, and long lifetimes. The dynamic characteristics and stability of the AMB system are actively controllable and closely related to the control parameters. The system support characteristics can be changed in real time during the working process by the control algorithm. Hence, the system may be designed to have better dynamic characteristics for control goals. In addition, AMBs can simplify the mechanical system construction and have self-adaptation and self-diagnostic capabilities [1,2,3]. AMBs have been used in many industrial fields, including vacuum and super-clean rooms, mechanical manufacturing (high-speed, high-precision machine tools), medical equipment (heart pumps), and turbomachinery (from small turbine molecular pumps to large megawatt turbine generators and compressors). A 300 MW class maglev turbine

generator [3] and a 700 MW class maglev blower [4] have been realized.

Under normal operating conditions, the rotor in the AMB system is levitated and the AMB control system maintains rotor dynamic responses to external disturbances and imbalances to be within a clearance gap, so there is no contact between the rotor and the touchdown bearings (TDBs). However, AMBs have limited load carrying capacity due to the magnetic field saturation. The following three conditions may cause contact between a levitated rotor and the TDBs [5]:

1. Large amplitude rotor motion around a critical speed.
2. Sudden increases in the imbalance of the rotor.
3. Large external disturbances experienced by the system (vibration, shock).

Turbomachinery can be considered as on-board machines in applications such as automotive turbochargers, maglev turbine generators used for nuclear plants, maglev centrifugal compressors mounted on floating production storage and offloading units [6], maglev pumps and refrigeration compressors on ships, and high-speed motors on electric aircraft or hybrid aircraft. In these cases, their bases are not fixed with respect to the ground. Depending on the application, these machines may experience severe dynamic inputs from, for example, shock loads, seismic waves, sea waves, and maneuvering. For an operational rotor-AMB-TDB system, these loads can lead to contact between the rotor and the TDBs, resulting in complex nonlinear vibrations and potential instabilities.

The dynamics of maglev systems excited by base motions have been studied in the open literature. Murai et al. [7] first studied the effect of earthquakes on a rotor-AMB system. Kasarda [8] studied, numerically and experimentally, the dynamic response of a non-rotational mass mounted on an AMB controlled by PID feedback and subjected to sinusoidal base motion. Clements [9] developed an AMB test rig to observe the rotor responses with base excitation. Some researchers have used feed-forward control to suppress base excited disturbances. Suzuki [10] designed an infinite impulse response (IIR) filter and a finite impulse response (FIR) filter in feed-forward control loops. The IIR filter reduced the rotor response by about 50% using a PID controller. Matsushita et al. [11] implemented a feed-forward compensator generating a signal proportional to the external acceleration for a PD controlled AMB system to reduce the vibrations generated by the Kobe earthquake. Sim et al. [12] proposed an angle feed-forward controller based on an inverse dynamic model and an acceleration feed-forward controller based on a normalized filtered-X LMS algorithm to effectively compensate for the disturbances. Kang et al. [13] limited the harmonic base motions of an electro-optical sight mounted on a moving vehicle by the same method. Sliding mode control was also applied to achieve good robust performance against parameter uncertainties and external disturbances [14]. Maruyama et al. [15] designed an efficient observer for a PD controlled AMB system that estimated the stator disturbances. The magnitude of the base shock disturbance was quite large and their duration extremely short. These

feed-forward controllers are effective for suppressing harmonic disturbances, but they are not as effective for base shock disturbances due to the inverse model error, system delays, and the convergence time of the adaptive feed-forward controller.

Keogh and Cole conducted a series of studies on the AMB controller design with base motion. Cole et al. [16,17] found that conventional PID controllers or PID controllers with synchronous imbalance suppression did not effectively prevent contact between the rotor and the TDBs. They then designed an H_∞ optimized controller to limit the rotor response. Keogh et al. [18] presented an H_∞ controller that allowed the designer to use cost functions to weight the two sources of excitation, then proposing a combined wavelet-H_∞ controller [19]. The wavelet transform decomposes the base excitation signal into hard and soft proportions for the H_∞ controller to minimize the transmitted forces and vibrations.

Calnetix Technologies in the US studied the effect of base motion on AMB systems, theoretically and experimentally. Hawkins studied the effect of shock machine testing on a gas turbine simulator supported by homopolar, permanent magnet bias magnetic bearings [20]. Saturation effects, clearance effects, and integrator and current limits were considered. However, the TDB model was simplified to a spring-damper structure without considering the inner race and ball motions with friction. Hawkins [21] conducted shock and vibration testing of an AMB supported energy storage flywheel. The results showed that shock isolators reduced the transmitted axial loads by 65%, and that a conventional controller could be used without a special design to ensure that the system ran stably without contact. Guo and Yu [22] also verified that the vibration response of a flexibly supported AMB system could be significantly reduced compared to that of a rigidly mounted system. Hawkins et al. [23] conducted vibration tests of an AMB supported compressor and compared the results with predictions. The compressor run stably without contact when it was placed on a U.S. Navy MIL-STD-167 shaker platform and driven at sinusoidal frequencies from 4 to 33 Hz at graduated displacements equal to a maximum of 1.5 G.

In the above studies, the dynamic responses of the rotor were limited without contact with the TDBs and the AMBs operated mainly in their linear region. The base motion accelerations were small, hence the vibration isolators reduced the energy transfer, and the AMBs were not saturated so that control algorithms such as PD feed-forward and H_∞ robust control algorithms could be designed to limit the rotor motion.

Some works have been dedicated to the case of rotor-TDB contact when the AMBs were still operating. Lawen and Flowers [24] investigated a synchronous interaction dynamics methodology to design TDBs. Keogh and Cole [25] analyzed the behavior of an imbalanced rotor in contact with the TDBs. The AMBs were simplified as spring/damper elements. Keogh and Cole [26] demonstrated that contact events from a linearly stable rotor orbit can drive the rotor into a nonlinear vibratory motion involving persistent contacts in which the phase of the measured vibration response may be

changed. Synchronous controllers designed to minimize the rotor vibration amplitudes may actually worsen the rotor response and create higher contact forces [19]. Inayat [27,28] considered nonlinear contact with the TDBs to derive bifurcation diagrams using a linear contact model with the TDBs simplified to a fixed hollow cylinder while ignoring the motions of the inner race and balls. Keogh [29] proposed active TDBs to help the rotor to recover from persistent contact. Jarroux [30] observed the dynamic behavior of AMB system with strong base motion. The 6000 rpm rotor, which was placed on a shock platform and experienced sinusoidal disturbance (0.1-1.1G amplitude and 20Hz frequency), returned to a stable state after rubbing with the TDBs for a short time. Hawkins et al. [31] presented Floating Shock Platform test results for an AMB supported chiller compressor for MIL-S-901D shock certification. After experiencing limited contact between the rotor and TDBs, the rotor returned to a stable operating state. Post-test inspections showed that the backup bearings had no raceway brinelling or other signs of distress.

An emergency shut-down procedure has been used to stop the machine to avoid uncontrolled behavior and structural damage when the motion of rotor is above a certain magnitude threshold [31,32]. In this situation, the dynamic problem of maglev system with a shock load is simplified to maglev rotor drop-down problem (with no controller). However, this is not practical for large turbomachines such as in nuclear plants, because the time to restart and recover normal operating conditions can be very long. If structural damage occurs, maintenance will incur significant costs [6].

Very few studies have given insights into interactions of the rotor-AMB-TDB system under shock loads while the AMBs are still operational, including consideration of the magnetic field saturation and nonlinear contact coupling. In such cases, the rotor may collide with the TDBs. The rotor-AMB system must deal simultaneously with conventional imbalanced forces, external base shocks, saturated electromagnetic forces and rotor-TDB interactions, which can trigger complex nonlinear rotor dynamics. This study presents nonlinear dynamics and parametric analysis of a rotor-AMB-TDB system under strong base shocks while the AMBs are still operating, to provide help for dynamic response predictions, core parameters designs and re-levitation controller designs.

2. Dynamic Modeling of the Rotor-AMB-TDB System

2.1 Rotor Model

A simplified rotor-AMB-TDB system including a rigid rotor, two radial AMBs and two TDBs is shown in Fig. 1. The rotor mass is concentrated to the disk located centrally on the rotor. The rotating machinery is assumed to be symmetric and, hence, the dynamic responses at the two bearings are identical and only the movement of rotor in

the $x-y$ plane is studied.

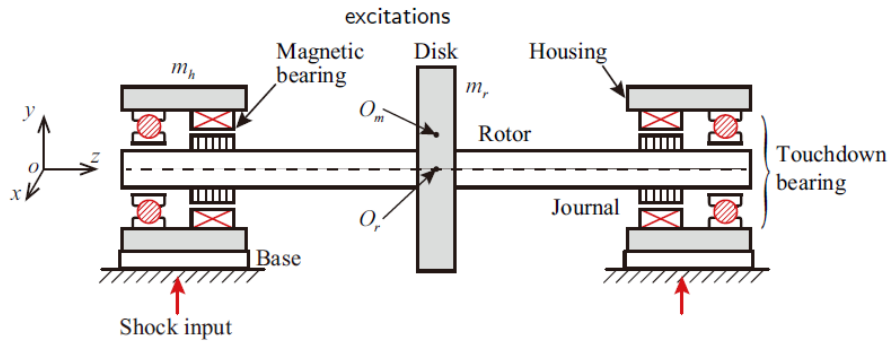

Figure 1: Schematic of the rotor-AMB-TDB system (massless shaft and rigid disk)

Since the rotor always has some residual unbalance, which is one of the key factors that cause vibrations, the force caused by the unbalanced mass is applied to the disk as an excitation force. The governing equation for the rotor with an instantaneous variable rotational speed $\omega = \dot{\theta}_r$ derived from Lagrange's equations is:

$$\mathbf{M}_r \ddot{\mathbf{q}}_r = \omega^2 \mathbf{Q}_1 + \dot{\omega} \mathbf{Q}_2 + \mathbf{F}_{\text{grav}} + \mathbf{F}_{\text{mag}} + \mathbf{F}_{\text{inner-r}}$$

$$\mathbf{M}_r = \begin{bmatrix} m_r & & \\ & m_r & \\ -m_r e \sin\theta_r & m_r e \cos\theta_r & J_c \end{bmatrix}, \mathbf{Q}_1 = \begin{bmatrix} m_r e \cos\theta_r \\ m_r e \sin\theta_r \\ 0 \end{bmatrix}, \mathbf{Q}_2 = \begin{bmatrix} m_r e \sin\theta_r \\ -m_r e \cos\theta_r \\ -m_r e^2 \end{bmatrix}$$

$$\mathbf{F}_{\text{grav}} = \begin{bmatrix} 0 \\ -m_r g \\ -m_r e g \cos\theta_r \end{bmatrix}, \mathbf{F}_{\text{mag}} = \begin{bmatrix} f_{\text{mag-x}} \\ f_{\text{mag-y}} \\ f_{\text{mag-x}} \cdot (y_r - y_h) - f_{\text{mag-x}} \cdot (x_r - x_h) \end{bmatrix}$$

$$\mathbf{F}_{\text{inner-r}} = \begin{bmatrix} -F_{n1} \cos\alpha + F_{t1} \sin\alpha \\ -F_{n1} \sin\alpha - F_{t1} \cos\alpha \\ f_{n1} e \sin(\alpha - \theta_r) - f_{t1}\left(r_r - e\cos(\alpha - \theta_r)\right) \end{bmatrix}, \alpha = \tan^{-1}\left(\frac{y_r - y_b}{x_r - x_b}\right)$$

where $\mathbf{q}_r = [x_r \quad y_r \quad \theta_r]^{\mathrm{T}}$ is the generalized coordinate vector, $\mathbf{M_r}$ is the mass matrix, and m_r and J_r are the mass and moment of inertia. On the right hand side, $\mathbf{Q}_1$ and $\mathbf{Q}_2$ are the force vectors caused by unbalanced mass; $\mathbf{F}_{\text{grav}}$ is the force of gravity; $\mathbf{F}_{\text{mag}}$ is support force from the AMBs, $F_{\text{mag-x}}$ and $F_{\text{mag-y}}$ are the magnetic forces in x, y directions which are described in Sec. 2.3; $\mathbf{F}_{\text{inner-r}}$ is the contact force

between the rotor and the inner race, including the normal contact force F_{n1} and the tangential contact force F_{t1}, which are described in Sec. 2.2. r_r and e are the rotor radius and eccentricity, and α is the angle between the centers of the rotor and the inner race.

2.2 Modeling of the TDB and Contact

Maglev rotating machinery typically uses deep groove ball bearings with or without cages as touchdown bearings. The simplified ball bearing model shown in Fig. 2 is used here for the bearing force calculation. The model ignores the centrifugal forces of the balls and assumes that the cage holds the balls precisely in their predefined positions. The outer race is rigidly fixed to the housing and the whole machine is rigidly mounted on the base. The base shock is assumed to act directly on the rotor-AMB-TDB system so that the effect of different of base shock inputs on system stability will become clear.

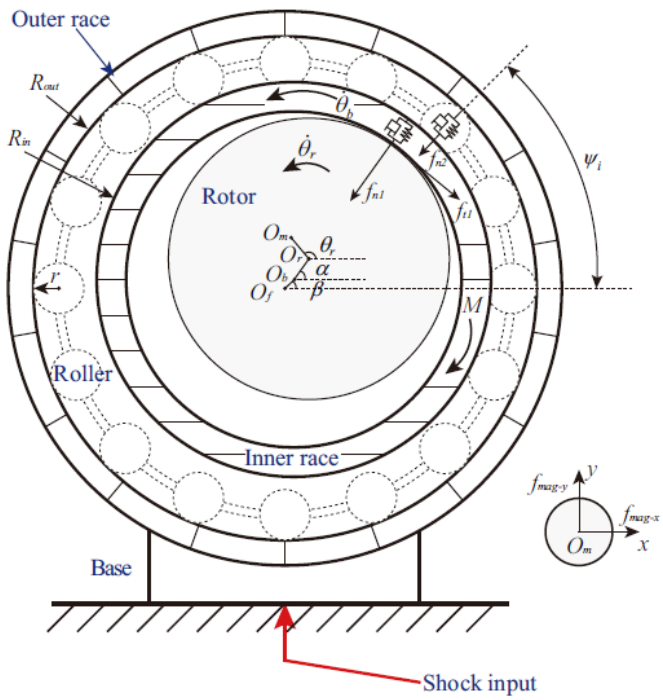

Figure 2: Rotor-TDB Model

The inner race of the bearing has two radial translational degrees of freedom (DOFs) and one rotational DOF around the center of the inner race [33, 34]. The governing equation for inner race is:

$$\mathbf{M}_b\ddot{\mathbf{q}}_b = \mathbf{F}_{\text{grav-b}} - \mathbf{F}_{\text{inner-r}} + \mathbf{F}_{\text{outer}}$$

$$\mathbf{M}_b = \begin{bmatrix} m_b & & \\ & m_b & \\ & & J_b \end{bmatrix}, \mathbf{F}_{\text{outer}} = \begin{bmatrix} -F_{n2}\cos\beta + (M / r_b)\sin\beta \\ -F_{n2}\sin\beta - (M / r_b)\cos\beta \\ -M \end{bmatrix}, \beta = \tan^{-1}\left(\frac{y_b - y_h}{x_b - x_h}\right)$$

where $\mathbf{q}_b = [x_b \quad y_b \quad \theta_b]^T$ is the generalized coordinates vector, $\mathbf{M_b}$ is the mass matrix and $\mathbf{F}_{\text{outer}}$ is the sum of the contact forces between the inner race and balls includes normal contact force, F_{n2}, and friction drag torque, M. β is the angle between the centers of the inner race and the outer race.

The radial contact force between the contact surfaces of the rotor and the inner race is evaluated based on the penalty function [35, 36, 37]. The normal contact force is given by

$$F_{n1} = \begin{cases} K_r \delta_r^{10/9} + C_r \dot{\delta}_r & , \delta_r > 0 \\ 0 & , \delta_r \le 0 \end{cases}$$

where δ_r is the penetration depth between the two contact points, $\dot{\delta}_r$ is the penetration velocity, and K_r and C_r are stiffness and damping coefficients, respectively, of the interaction between the rotor and inner race.

For the circle-in-circle contact model, the penetration depth δ_r is expressed as

$$\delta_r = \sqrt{(x_r - x_b)^2 + (y_r - y_b)^2} - r_0$$

where r_0 is the radial clearance between the rotor and inner race of the TDB.

The contact stiffness K_r depends on the geometry and the rotor and bearing materials. For a line contact, K_r is given by [38]

$$K_r = \left\{ \frac{0.39^{10/9}}{l} + \left[\frac{4(1-\upsilon_1^2)}{E_1} + \frac{4(1-\upsilon_2^2)}{E_2} \right] \right\}^{-1}$$

where E is the elasticity modulus and υ is Poisson's ratio. The subscripts (1 and 2) represent the two contact surface materials.

The collision damping coefficient is expressed as

$$C_r = \mathrm{STEP}\left(\delta_r, 0, 0, \delta_{\max}, C_{r-\max}\right)$$

where $\delta_{\max}$ is the allowable maximal penetration and $C_{r-\max}$ is the maximal damping during contact. The STEP function is defined as

$$\mathrm{STEP}(x, x_0, h_0, x_1, h_1) = \begin{cases} h_0 & x \le x_0 \\ h_0 + (h_1 - h_0)\eta^2(3-2\eta) & x_0 < x < x_1 \\ h_1 & x \ge x_0 \end{cases}$$

with $\eta = (x - x_0)/(x_1 - x_0)$.

The tangential friction force is calculated by Coulomb's Friction Law as

$$F_{t1} = \mu\left(v_t\right) F_{n1}$$

where the coefficient of friction, μ, is

$$\mu\left(v_t\right) = \begin{cases} -\mathrm{sign}\left(v_t\right)\cdot\mu_d & \left|v_t\right| > v_d \\ \mathrm{sign}\left(v_t\right)\mathrm{STEP}\left(\left|v_t\right|, v_d, \mu_d, v_s, \mu_s\right) & v_s \le \left|v_t\right| \le v_d \\ \mathrm{STEP}\left(v_t, -v_s, -\mu_s, v_s, \mu_s\right) & \left|v_t\right| < v_s \end{cases}$$

where $v_t = \omega \cdot r + v_r - \dot{\theta}_b r_b$ is the relative velocity between the rotor and the inner race at the contact point in which v_r is the relative velocity of center of the rotor and inner race, v_s and v_d are the static and dynamic transition velocities, and μ_s and μ_d are the static and dynamic friction coefficients.

The contact force between ball i and the inner race is described by a nonlinear Hertzian contact model with dissipation [39] as:

$$F_{ni} = \begin{cases} K_b \delta_i^{3/2} + C_b \dot{\delta}_i & \delta_i > 0 \\ 0 & \delta_i \le 0 \end{cases}$$

where K_b and C_b are the stiffness and damping coefficients for the contact between ball i and the inner race. δ_i is the contact penetration depth and $\dot{\delta}_i$ is the penetration velocity. The stiffness coefficient K_b in Eq. (10) is a function of the inner and outer race contact as:

$$K_b = \left(\left(\frac{1}{K_b^{in}} \right)^{2/3} + \left(\frac{1}{K_b^{out}} \right)^{2/3} \right)^{-3/2}$$

where K_b^{in} and K_b^{out} are calculated using generalized expressions for elliptic integrals and an ellipticity parameter based on the elliptical contact conjunction between the two solids. The damping coefficient is calculated by Eq. (6).

There is clearance r_{cl} between the ball and the inner race in the radial direction of the bearing. The contact penetration depth can be expressed as

$$\delta_i = 2r + R_{in} - R_{out} + (x_b - x_h)\cos\psi_i + (y_b - y_h)\sin\psi_i - r_{cl}$$

where r is the ball radius, R_{out} is the outer raceway radius, R_{in} is the inner raceway radius, and ψ_i is the attitude angle of ball i.

Finally, the resultant radial bearing forces acting between the inner race and balls can be summarized as:

$$F_{n2} = \sum_{i=1}^{z} F_{ni} \cos(\psi_i - \beta)$$

where z is the number of balls in the TDB.

The friction drag torque M inside the bearing is given by Palmgren's empirical formula [36, 38]:

$$M = M_0 + M_1,$$

$$M_0 = \begin{cases} 10^{-7} f_0 \left(v_0 \dot{\theta}_b\right)^{2/3} d_m^3 & v_0 \dot{\theta}_b > 2000 \\ 160 \times 10^{-7} f_0 d_m^3 & v_0 \dot{\theta}_b \le 2000 \end{cases}$$

$$M_1 = f_1 + P_1 + d_m$$

where M_0 is the friction torque due to the bearing lubricant viscosity and the inner race speed, M_1 is the friction torque due to external loads on the bearing, f_0 is a factor depending on the bearing type and lubrication, v_0 is the kinematic viscosity of the lubricant, $\dot{\theta}_b$ is the angular velocity of the inner race, f_1 is a factor depending on the bearing design and the relative bearing load, and P_1 is the equivalent dynamic load.

2.3 Modeling of the AMB and Controller

The electromagnetic force near the static equilibrium position is calculated using a linearized model [3]:

$$F = F_+ - F_- = \frac{\mu_0 n^2 A}{4}\left[\frac{\left(i_0 + i\right)^2}{\left(s_0 - \Delta\right)^2} - \frac{\left(i_0 - i\right)^2}{\left(s_0 + \Delta\right)^2}\right]\cos\eta \approx \frac{\mu_0 n^2 A i_0}{s_0^2}\cos\eta \cdot i + \frac{\mu_0 n^2 A i_0^2}{s_0^3}\cos\eta \cdot \Delta = k_i i + k_\Delta \Delta$$

where k_Δ is the force-displacement coefficient, and k_i is the force-current coefficient. η is the angle between the electromagnetic force and the magnetic pole. s_0 is the gap between the rotor and AMB when the rotor is in the ideal center, i_0 is the bias current, μ_0 is the vacuum permeability, n is the number of coil turns, and A is the magnetic pole area. i is the current in the coil amplifier output. Δ is the rotor displacement at the x and y direction at the bearing support point, $\Delta = x_r, y_r$.

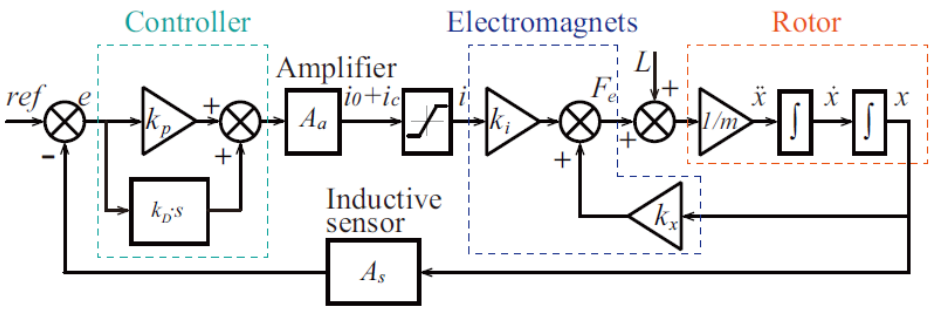

Figure 3: Control diagram for the single DOF AMB system

Figure. 3 shows a single DOF AMB feedback control loop. e is the displacement error which indicates the difference between the actual position and the equilibrium position, i_c is the PD controller current output , F_e is the electromagnetic force, L is the external disturbance force, A_s is the inductive sensor gain coefficient, and A_a is the power amplifier gain coefficient. The AMB magnetic field is assumed to be saturated. The electromagnetic force in the AMB at each DOF is controlled by the PD control at each calculational step during the solution. The equivalent stiffness, k_e, and damping, c_e, in the frequency domain are

$$\begin{cases} k_e = k_i k_p A_a A_s - k_\Delta \\ c_e = k_i k_d A_a A_s \end{cases}$$

3. Numerical Solution

The mathematical model for the rotor-AMB-TDB system may be solved numerically to predict the response for the base shock excitation for various parameters.

3.1 Time-domain Shock Excitation

The shock analysis in the time domain is based on the BV043/85 criterion [40, 41]. The shock excitation in this standard is given in the form of the shock response spectrum (SRS) given in Fig. 4(a). The SRS parameters meet the following conditions:

$$f_1 = \frac{V_0}{2\pi \cdot D_0}, \; f_2 = \frac{A_0}{2\pi \cdot V_0}$$

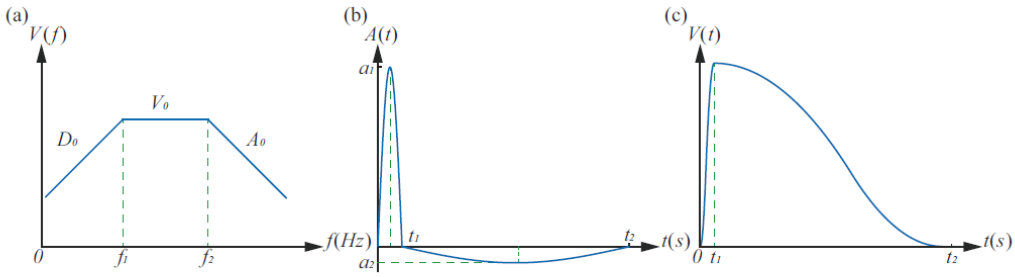

Figure 4: Relationship between design shock spectrum and the time-domain shock excitation (a) design shock spectrum, (b) plus-minus half-sine acceleration wave, (c) velocity curve

The design shock spectrum of the BV043/85 criterion can be transposed to an equivalent acceleration time-domain curve having a plus-minus half-sine acceleration wave as shown in Fig. 4(b). The time-domain curve of the velocity in Fig. 4(c) can be obtained by integration. The velocity should decrease to zero at the end of shock so that the areas under two triangles are equal. The SRS parameters of the plus-minus half-sine acceleration wave from the design shock spectrum for the BV043/85 standard are:

$$a_1 = 0.5A_0$$
$$t_1 = 2\pi V_0 / 3A_0$$
$$a_2 = \pi V_0 / (t_2 - t_1)$$
$$t_2 = 3D_0 / V_0 + t_1$$

The time-domain shock excitation is then a function of the frequencies, f_1 and f_2, and the acceleration, A_0. The governing equation for the housing is

$$\mathbf{M}_h \ddot{\mathbf{q}}_h = \mathbf{F}_{shock}(t)$$

where $\mathbf{M}_h$ is the housing mass matrix and $\mathbf{F}_{shock}$ is the base shock excitation given by the curve in Fig. 4(b).

This section gives the dynamic responses of rotor with a rotational speed $\omega = 500$ Hz (30,000 rpm) and base shocks with accelerations, A_0, from 0 G to 20 G for $f_1 = 10$ Hz and $f_2 = 80$ Hz. As an example, the time-domain values of a_2, t_1, t_2 and the final lift height of the base, h, corresponding to the shock acceleration peaks $a_1 = 3\,\text{G}, 10\,\text{G}, 20\,\text{G}$, are listed in Table 1.

Table 1
Time-domain parameters of shock excitation

a_1 (G)	a_2 (G)	t_1 (s)	t_2 (s)	h (mm)
3	-0.44	0.0042	0.0519	2.03
10	-0.87	0.0042	0.0519	6.75
20	-1.75	0.0042	0.0519	13.51

3.2 Simulation Configuration

Reliable structural parameters are needed to accurately predict the dynamic behavior. Structural and contact parameters in the literature [36, 42, 43] were used in the simulations. The rotor, AMB, and TDB (deep groove ball bearings with a cage) parameters are listed in Table 2. The parameters for the contact between rotor and TDB with a cage are listed in Table 3. The numerical model was verified by comparing the predicted results with measured data for a drop down event.

The rotor levitated by the AMBs was driven by the frequency converter to the rated speeds and operated from a transient state to steady-state (forward whirling caused by residual unbalanced force) in the first four seconds. Then, the rotor-AMB-TDB system was subjected to the base shocks with various acceleration peak value from the programmed shock table. The motions of rotor, TDB and base were then predicted by numerically integrating the system equations using the integrator ode45 in MATLAB, which is based on an explicit Runge-Kutta (4,5) formula. The relative and absolute error tolerances are set as 10^{-6} and 10^{-9}, respectively. The numerical calculations were all converged.

Table 2
Rotor, AMB and TDB's structural parameters

Parameters	*Value*
Rotor mass, m_r	11.5 kg
Unbalance eccentricity, e	2×10^{-3} mm
Rotor polar moment of inertia, J_r	5.81×10^{-3} kg · m^2
Rotor radius, r_r	19.85 mm
Air clearance between rotor and inner race, r_0	0.15 mm
Mass of inner race, m_b	0.048 kg
Inner radius of inner race, r_{inner}	20 mm
Polar moment of inertia of inner race, J_b	2.33×10^{-5} kg · m^2
Ball diameter, d_{ball}	5.5 mm
Number of balls, z	19
Bearing width, B	12 mm
Clearance between the ball and outer race, r_{cl}	0.01 mm
Outer race diameter, d_{outer}	62 mm
Mass of outer race, AMB, stator and housing M_h	80.96 kg
Force-displacement coefficient, k_s	4.32×10^8 N/m
Force-current coefficient, k_i	2.16×10^4 N/A
Power amplifier gain, A_a	1 A/V
Inductive sensor gain, A_s	25000 V/m

Table 3
Contact parameters of rotor and TDB

Parameters	*Value*
Stiffness coefficient between the rotor and inner race, K_r	1.988×10^9 N/m
Maximum damping coefficient between the rotor and inner race, C_{r-max}	1000 N·s/m
Static critical speed, v_s	0.1 m/s
Dynamic critical speed, v_d	0.1 m/s
Static friction coefficient, μ_s	0.1
Dynamic friction coefficient, μ_d	0.1
Stiffness coefficient between the inner race and ball, K_b	7.81×10^9 N/m
Maximum damping coefficient between the inner race and ball, C_{b-max}	750 N·s/m
Friction drag torque, M	0.1 N·m
Maximum permitted penetration, δ_{max}	10^{-5} m

4. Bifurcation and Nonlinear Dynamics Analysis

Due to the high nonlinearity of the rotor-AMB-TDB system, the nonlinear behavior was investigated numerically and is discussed here in detail. Section 4.1 discuss dynamic behavior with typical base shock accelerations and Section 4.2 presents bifurcation analysis of some the main parameters.

4.1 Dynamic behavior for typical base shock accelerations

With the establishment of the dynamic model in Section 2 and the parameters in Section 3.2, dynamic responses of the rotor-AMB-TDB system disturbed by a series of base shocks in accordance with BV043/85 with peak accelerations from 1G-20G were predicted. Different responses were observed in the simulations under three typical base shock responses, which are shown in Figs. 5-7.

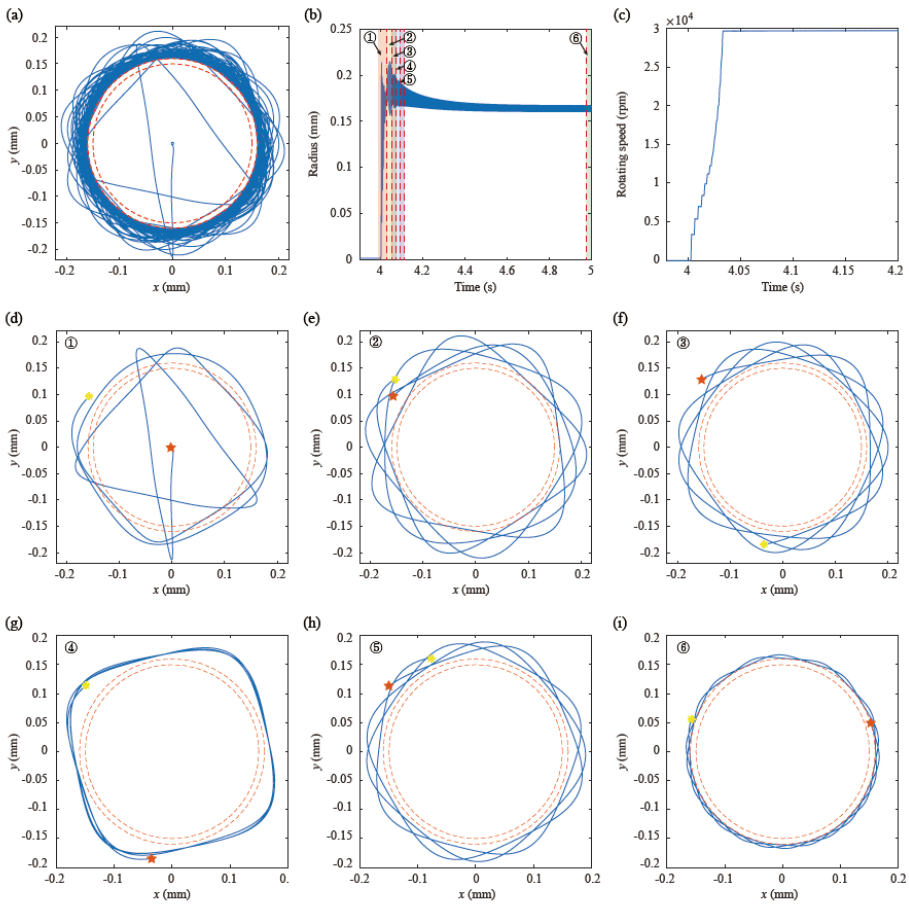

Figure 5: Dynamic behavior of the system subjected to a 10 G base shock with $e = 2 \times 10^{-6} m$. (a) rotor trajectory from 3.8 s to 5 s; (b) radius of the trajectory from the nominal center of the rotor; (c) rotational speed of the inner race of TDB; (d)-(i) staged trajectory: (d) 3.99 s-4.03 s, (e) 4.03 s-4.05 s, (f) 4.05 s-4.07 s, (g) 4.07s-4.09 s, (h) 4.09 s-4.11 s, (i) 4.96 s-5 s.

Figure 5 shows the dynamic behavior of the system with $\omega = 30,000$ rpm, $k_e = 1\times10^6$ N/m, $\xi_e = 0.01$, $r_0 = 0.15$ mm, and $e = 2\times10^{-6}$ m subjected to a base shock with a peak acceleration of 10G. The rotor trajectory in Fig. 5(a) and the motion radius in Fig. 5(b) show that the rotor whirls forward with a very small motion radius of motion of 2×10^{-6} m before the base shock. The rotor then rebounds sharply at about 0.1 s after the base shock with the motion then evolving into a continuous dry

whirl with a large radius of motion. The evolution of the movement is shown by the rotor trajectories at 6 different times in Fig. 5(d)-(i). In each figure, the smaller red circle indicates the nominal size of the radial clearance while the larger red circle indicates the nominal size of the radial clearance after considering the clearance between the inner race and the balls. The star marks the beginning of the trajectory, while the snowflake marks the end. In the early part of the shock response, the rotor partially collides with the TDB with large interaction forces, resulting in a large penetration. However, the rebound time period is very short and the rotor motion quickly evolves into a transient backward dry whip. Later, the normal and tangential contact forces, the imbalanced force and the saturated electromagnetic force cause the rotor to enter into a steady continuous backward dry whirl, whose trajectory approximates a circle with the air clearance as its radius. The rotational speed of the inner race of the TDB is shown in Fig. 5(c). After the inner race and the rotor come into contact, the rotational speed increases rapidly, reaching about 29,730 rpm which is close to the rotor speed of 30,000 rpm after about 0.035 seconds. The small speed difference is due to the inner diameter difference between the rotor and the inner race.

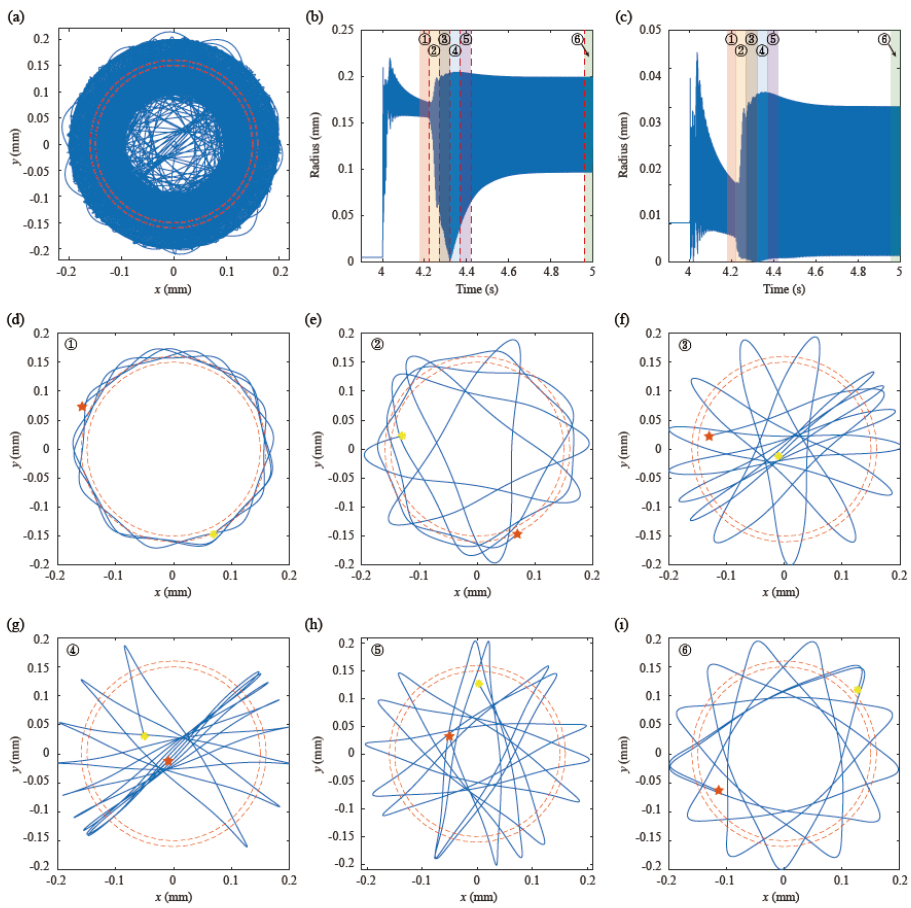

Figure 6: Dynamic behavior of the system subjected to 10 G base shock with $e = 4.8 \times 10^{-6} m$. (a) rotor trajectory from 3.8 s to 6 s; (b) radius of the trajectory from the nominal center of the rotor; (c) radius of the inner race of TDB; (d)-(i) staged trajectory: (d) 4.18 s-4.22 s, (e) 4.22 s-4.27 s, (f) 4.27 s-4.32 s, (g) 4.32 s-4.37 s, (h) 4.37 s-4.42 s, (i) 4.96 s-5 s.

Figure 6 shows the dynamic behavior of the system with $\omega = 30,000$ rpm ,

$k_e = 1.5\times10^6$ N/m , $\xi_e = 0.01$, $r_0 = 0.15$ mm , and $e = 4.8\times10^{-6}$ m subjected to a base shock with a peak acceleration of 10G. The rotor trajectories and motion radii in Figs. 5 and 6 are similar in the early stage of the contact. The rotor experiences sharp rebounds about 0.1 s after the base shock with the motion then evolving into a state that combines dry whip and dry whirl. However, this state does not last long. At 0.22 s after the base shock, the rotor motion radius suddenly increases. The rotor trajectory in Fig. 6(a) and the inner race motion radius variation in Fig. 6(c) shows that the level of the rotor and the inner race vibration intensifies with rotor amplitudes and contact force suddenly increasing. These violent vibrations would continue if there is no external intervention. The evolution of the movement is shown by the rotor trajectories at 6 different times in Fig. 6(d)-(i). The rotor motion evolves from the combination of dry whip and dry whirl to the severe collision and finally steady continuous rebounds. The frequency evolution during this process is analyzed in Sec. \ref{sec:4.2.2}.

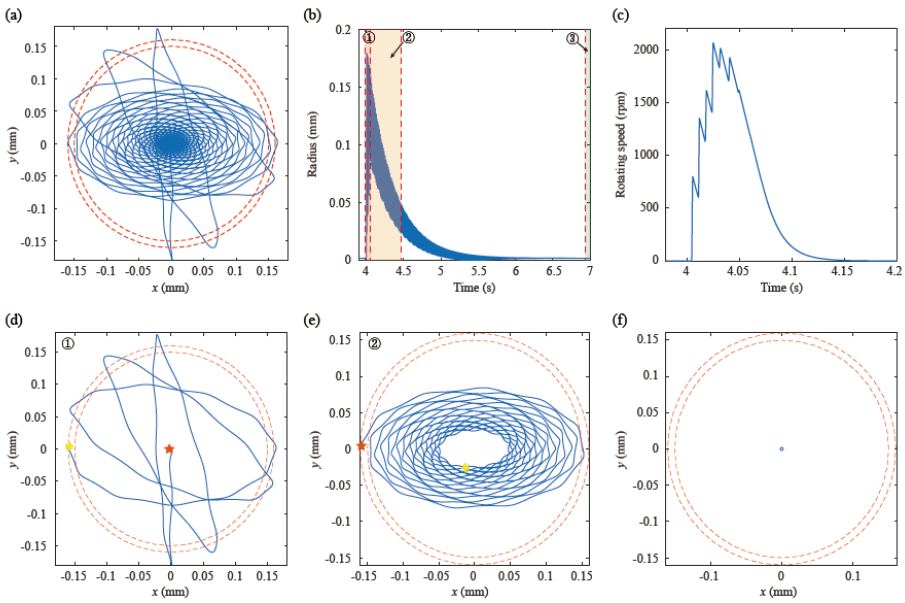

Figure 7: Dynamic behavior of the system subjected to 3 G base shock. (a) rotor trajectory from 3.8 s to 7 s; (b) radius of the trajectory from the nominal center of the rotor; (c) rotational speed of the inner race of TDB; (d)-(f) staged trajectory: (d) 3.97 s-4.05 s, (e) 4.05 s-4.45 s, (f) 6.92 s-7 s.

Figure 7 shows the dynamic behavior of the system with $\omega = 30,000$ rpm , $k_e = 1\times10^6$ N/m , $\xi_e = 0.01$, $r_0 = 0.15$ mm , and $e = 2\times10^{-6}$ m subjected to a base shock with a peak acceleration of 3G. The rotor again experiences sharp rebounds at about 0.1 second after the base shock, but the contact does not last long. The rotor then gradually recovers to the center with the original whirl radius. The rotor trajectories at 3 time periods are shown in Fig. 7(d)-(f). The initial shock response is similar to the 10G shock response with the rotor partially colliding with the TDB. However, in this case, the rotor returns to the original small whirl state with a backward whirl. The recovery time is related to the controller parameters. Thus, the contact occurs only over

a very short limited time with a transition to a backward whirl instead of the forward whirl after the base shock. The rotational speed of the inner race of the TDB is shown in Fig. 7(c). After the inner race and the rotor come into contact, the inner race rotational speed increases rapidly. However, the inner race rotational speed returns to 0 rpm due to the short, limited contact time and the friction from balls.

These responses illustrate three typical shock responses. These three motion modes can be concluded qualitatively as follows:

1. Transient sharp rebounds + transient backward dry whip + continuous backward dry whirl.
2. Transient sharp rebounds + combined backward dry whip and dry whirl + continuous rebounds.
3. Transient sharp rebounds + recovery to the center with the original whirl radius.

The dry friction tangential forces are responsible for the backward dry whip/whirl. The second mode only occurs when the rotor has a large residual imbalance with the parametric analysis for this behavior presented in Section 4.2.2.

4.2 Bifurcation and Parametric Analysis

Bifurcation diagrams are useful for observing nonlinear dynamic behavior. This section analyzes the bifurcation with the radial clearance, unbalance eccentricity, equivalent stiffness, equivalent damping ratio, and initial rotor position. The analyses use the time series data of the last 200 time intervals $T = 2\pi / \omega$, that is the driven rotor period in this non-autonomous system, to ensure that the data used represents the steady-state conditions. The data are then used to generate the rotor trajectory, frequency spectra, Poincaré maps, and bifurcation diagrams.

The rotor motion can be seen directly from the rotor trajectory. A Fast Fourier transformation (FFT) is used to obtain the frequency spectra of the rotor center relative to the housing in the horizontal and vertical directions. To generate a Poincaré map, a Poincaré section that is transverse to the flow of a given dynamic system is considered. A point on this section is a return point of the time series at the constant time interval of T. The projection of the Poincaré section on x-y plane is related to the Poincaré map of the dynamic system. The points on Poincaré map are used to draw the bifurcation diagram in various system parameters [44, 45].

4.2.1 Bifurcation of the air clearance

The radial clearance between the rotor and the TDB is an important structural design

parameter in maglev rotating machinery. The design suitability can directly affect the rotor motion mode after the base shock.

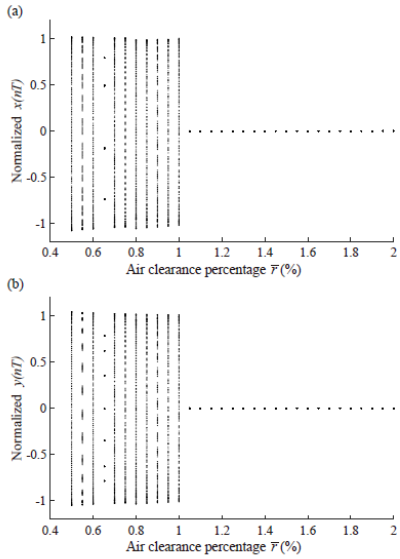

Figure 8: Bifurcation diagrams of the air clearance percentage, $\bar{r}$: (a) x(nT), (b) y(nT), (a_1 = 10 G, ω = 500 Hz(30,000 rpm), $k_e = 1\times10^6$ N/m, $\xi_e = 0.01$, $e = 2\times10^{-6}$ m)

Figure 8 shows the bifurcation diagrams of the rotor motion in the horizontal and vertical directions versus the radial clearance ($r_0 = 0.1$ mm-0.4 mm) between the rotor and the TDB. The horizontal axis is the percentage radial clearance relative to the TDB inner radius, $\bar{r} = r_0 / r_{\text{inner}}$. The results show that for radii less than $r_0 = 0.2$ mm ($\bar{r} = 1\%$), the system is irregular. Figure 9(a)-(c) demonstrate the rotor trajectory, Poincaré map and frequency spectrum for $r_0 = 0.1$ mm ($\bar{r} = 0.5\%$), respectively. The steady-state trajectory shows a quasi-periodic motion. The major frequency of 85 Hz is the backward dry whirl frequency caused by the continuous contact between the rotor and the TDB, while 500 Hz is the rotor rotational frequency. $7T$ periodic behavior can be found at $r_0 = 0.13054$ mm ($\bar{r} = 0.6527\%$) as shown in Fig. 9(d)-(f) as the rotation frequency of 500 Hz is seven times the backward dry whirl frequency of 71.4 Hz. The analysis for $r_0 = 0.16$ mm ($\bar{r} = 0.8\%$) also demonstrates quasi-periodic motion. The main frequency component, the backward dry whirl frequency, is 62.5 Hz. There are two additional frequencies that have small peaks besides the rotation and backward whirl frequencies. The frequency of 220 Hz comes from the inner race excitation, while the frequency of 345 Hz is the superposition of twice the backward whirl frequency and the inner race excitation response frequency. This multi-frequency case occurs in the range of $r_0 = 0.16$ mm-0.2 mm ($\bar{r} = 0.8\% - 1\%$).

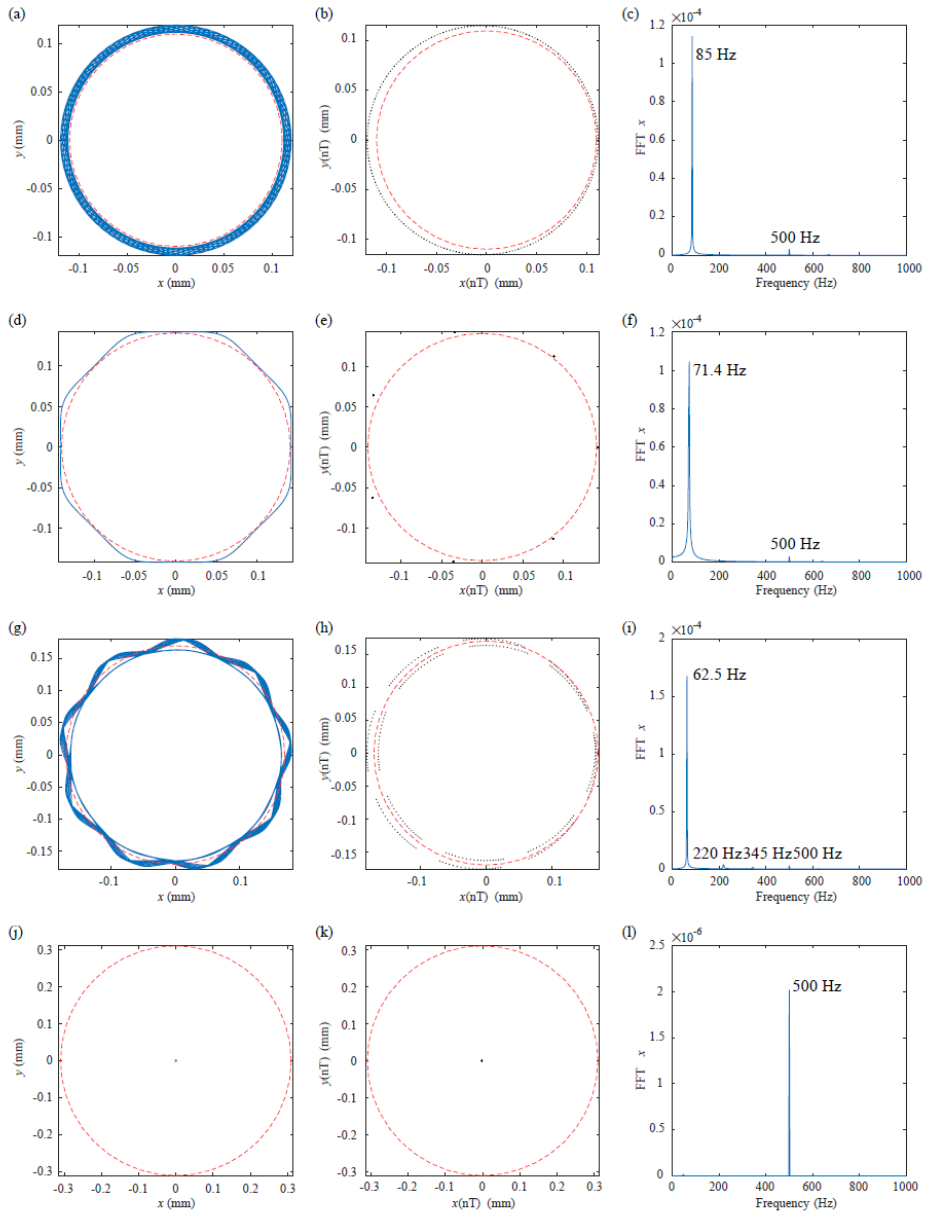

Figure 9: Dynamic analysis for the air clearance r_0. (a)(b)(c): rotor trajectory, Poincaré map and frequency spectrum for $r_0 = 0.1$ mm; (d)(e)(f): rotor trajectory, Poincaré map and frequency spectrum for $r_0 = 0.13054$ mm; (g)(h)(i): rotor trajectory, Poincaré map and frequency spectrum for $r_0 = 0.16$ mm; (j)(k)(l): rotor trajectory, Poincaré map and frequency spectrum for $r_0 = 0.3$ mm

For percentages greater than 1% (corresponding to $r_0 > 0.2$ mm), the steady-state shock response exhibits periodic motion. Figure 9(j)-(l) show the rotor trajectory, Poincaré map and frequency spectrum for r_0 is 0.3 mm ($\bar{r} = 1.5\%$), respectively. The steady-state trajectory is a 500 Hz backward whirl with the original small whirl radius, which is caused by the rotor imbalance excitation. There is only one point at the Poincaré section in this case.

In addition, the analysis indicates that the rotor backward dry whirl frequency decreases

from 85 Hz to 52.5 Hz with the air clearance increasing from 0.1 mm to 0.2 mm ($\bar{r} = 0.5\% - 1\%$). Thus, a larger radial clearance leads to a smaller backward whirl/whip speed and allows the rotor to be more easily pulled back to the center by the electromagnetic forces. However, a large radial clearance also increases the gap between the AMB and the rotor, which increases the nonlinearity of the electromagnetic forces and increases the AMB volume. Therefore, a reasonable design of the radial clearance is extremely important when designing high performance maglev rotating machinery that can withstand large shocks.

4.2.2 Bifurcation of the unbalance eccentricity

Residual imbalanced mass of the rotor is the main source of synchronous vibrations in traditional rotating machinery. In maglev rotating machinery, the synchronous vibrations can be eliminated by active control based on feed-forward compensation or filtering, which reduces the rotor dynamic balance requirements to a certain extent. However, the rotor dynamic balance still affects the dynamic behavior of the rotor in contact with the TDB. This section presents the effect of the rotor with various unbalance eccentricities.

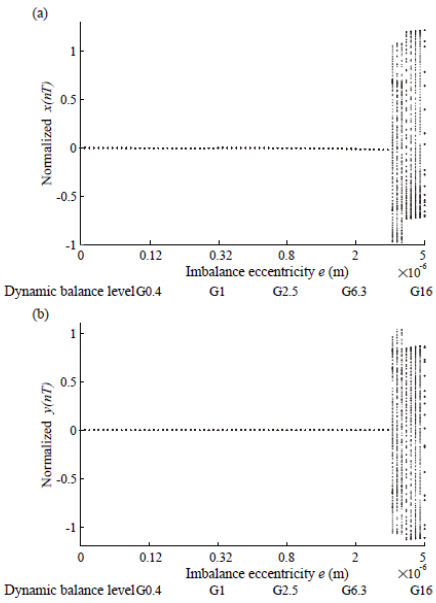

Figure 10: Bifurcation diagrams the unbalance eccentricity, e: (a) x(nT), (b) y(nT), ($a_1 = 10\ G$, $\omega = 500$ Hz(30,000 rpm), $k_e = 1.5 \times 10^6$ N/m, $\xi_e = 0.01$, $r_0 = 0.15$ mm)

Figure 10 shows the bifurcation diagrams of the rotor motion in the horizontal and vertical directions versus the eccentricity ($e = 0 - 5 \times 10^{-6}$ m). The horizontal axis is the unbalance eccentricity which is divided into 5 parts according to the dynamic balance level. The eccentricity in each part is distributed evenly at equal intervals.

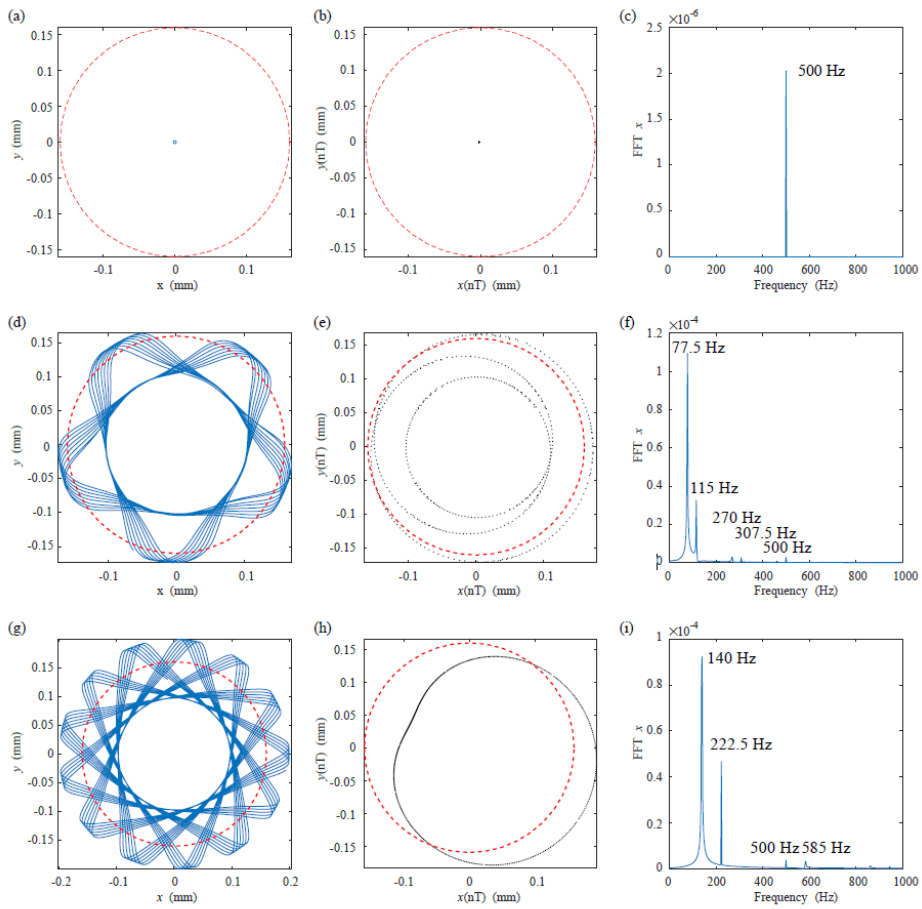

Figure 11: Dynamic analysis for the unbalance eccentricity, e. (a)(b)(c): rotor trajectory, Poincaré map and frequency spectrum for $e = 2 \times 10^{-6}$ m; (d)(e)(f): rotor trajectory, Poincaré map and frequency spectrum for $e = 3.6 \times 10^{-6}$ m; (g)(h)(i): rotor trajectory, Poincaré map and frequency spectrum for $e = 4.8 \times 10^{-6}$ m

When the eccentricity is less than $e = 3.6 \times 10^{-6}$ m, the steady-state shock response shows periodic motion. Figure 11(a)-(c) demonstrate the rotor trajectory, Poincaré map and frequency spectrum for $e = 2 \times 10^{-6}$ m, respectively. The steady-state trajectory is a 500 Hz backward whirl with the original small whirl radius caused by rotor imbalance excitation. There is only one point in the Poincaré section in this case which shows that a maglev rotor with an unbalance eccentricity smaller than $e = 3.6 \times 10^{-6}$ m can recover to a whirl with the original radius after a strong 10G base shock as shown in Fig. 7.

When the eccentricity is larger than $e = 3.6 \times 10^{-6}$ m, the system response is irregular and has multiple frequencies. The instabilities can be divided into those:

1. With relatively low rebound frequency ($e = 3.6 \times 10^{-6} - 4 \times 10^{-6}$ m);

2. With relatively high rebound frequency ($e = 4\times10^{-6} - 5\times10^{-6}$ m).

Figure 11(d)-(f) show the rotor trajectory, Poincaré map and frequency spectrum for $e = 3.6\times10^{-6}$ m, respectively. The steady-state trajectory is a quasi-periodic motion with rebound. The major frequency components of 77.5 Hz is the backward rebound frequency caused by the continuous interaction between the rotor and the TDB while 115 Hz comes from the inner race excitation. The instability of the inner race is induced by the rotor during the transition from the initial 500 Hz synchronous forward whirl to the low-frequency asynchronous backward whirl which then affects the rotor dynamic behavior in turn. Compared with Fig. 11(g), the system has less collisions during the same time. The 270 Hz is the result of the superposition of twice the rebound frequency and the inner race excitation response frequency. The 307.5 Hz is the result of the superposition of twice the inner race excitation response frequency and the rebound frequency. The system for $e = 4.8\times10^{-6}$ m also exhibits quasi-periodic motion. The main frequency components are 140 Hz which is the backward rebound frequency and 222.5 Hz, which is the response frequency of inner race excitation. The system has a higher rebound frequency than in Fig. 11(d). The 500 Hz is the rotor rotational frequency. The 585 Hz is the superposition of twice the inner race excitation response frequency and the rebound frequency.

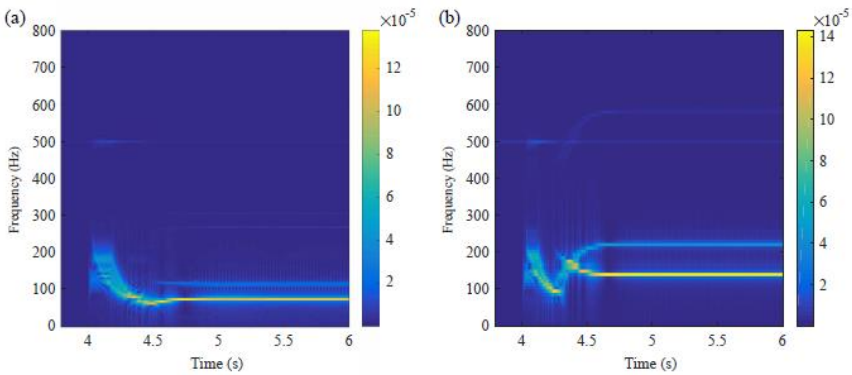

Figure 12: Short time Fourier transform (STFT) (a): $e = 3.6\times10^{-6}$ m, (b): $e = 4.8\times10^{-6}$ m

The analysis above is for the steady-state behavior. The results in Fig. 6 indicate a behavior evolution process. The evolution of the rotor frequency over time can be analyzed using Short Time Fourier Transforms (STFT) with the results shown in Fig. 12. After the base shock occurs, the rotor frequency decreases down to a critical point and then suddenly increases. For the rotor with the 3.6×10^{-6} eccentricity, after the rotor frequency drops to 64 Hz at 4.48 s, the rotor frequency jumps to 77.5 Hz. The inner race was excited to vibrate at 115 Hz at this time. For the rotor with the 4.8×10^{-6}

eccentricity, after the rotor frequency drops to 88 Hz at 4.26 s, the rotor frequency jumps to 140 Hz and the inner race is excited to vibrate at 222.5 Hz. The frequency for this sudden increase is related to the rotor-AMB-TDB system parameters.

Although active self-balancing control can reduce the influence of rotor imbalance, better balancing improves rotor recovery after a base shock.

4.2.3 Bifurcation of the equivalent stiffness and damping ratio

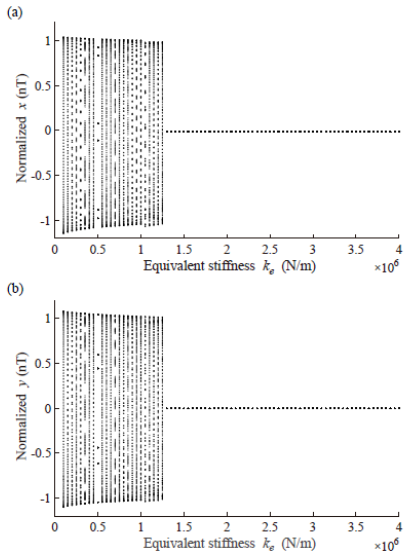

Figure 13: Bifurcation diagrams of the equivalent stiffness, k_e: (a) x(nT), (b) y(nT);($a_1 = 10\ G$, $\omega = 500$ Hz(30000 rpm), $r_0 = 0.15$ mm, $\xi_e = 0.01$, $e = 2 \times 10^{-6}$ m)

By considering the equivalent stiffness as a parameter of the system, qualitatively different behavior can be observed in Fig. 13 in the range $1\times10^5 \le k_e \le 4\times10^6$ N/m. The results show that for stiffness less than $k_e = 1.25\times10^6$ N/m, the system is irregular. Figure 14(a)-(c) demonstrate the rotor trajectory, Poincaré map and frequency spectrum for $k_e = 2\times10^5$ N/m, respectively. The steady-state trajectory is in quasi-periodic motion. The major frequency of 109 Hz is the backward dry whirl frequency caused by the continuous contact between the rotor and the TDB while 500 Hz is the rotor rotational frequency. Fig. 14(d)-(f) show similar analysis for $k_e = 5.024\times10^5$ N/m. 6 T periodic behavior can be found as rotor rotational frequency of 500 Hz is about six times the backward dry whirl frequency of 83.3 Hz. The analysis for $k_e = 1.15\times10^6$ also show quasi-periodic motion with two additional frequencies besides rotation and

backward dry whirl frequencies. The 220 Hz response comes from the excitation of inner race motion while the 345 Hz response is the superposition of twice the backward whirl frequency and the inner race excitation response. Multiple frequencies occur for the range of $1.05\times10^6 \le k_e \le 1.25\times10^6$ N/m with the low frequency from the backward dry whirl motion of the rotor still being the main frequency component.

For stiffness greater than $k_e = 1.25\times10^6$ N/m, the rotor response is periodic motion in both the horizontal and vertical directions. The maglev rotor with the equivalent support stiffness in this range can recover from a strong 10G base shock to whirl with the original radius as seen in Fig. 7. Theoretically, the rotor can avoid the backward dry whirl and dry whip attracting. Figure 14(j)-(l) demonstrate the rotor trajectory, Poincaré map and frequency spectrum for $k_e = 2\times10^6$ N/m, respectively. The steady-state trajectory is a 500 Hz backward whirl with the original small whirl radius caused by rotor imbalance excitation. There is only one point in the Poincaré section in this case.

In addition, the analysis indicate that the backward dry whirl frequency of the rotor decreases from 125 Hz to 60 Hz with the equivalent stiffness increasing from 1×10^5 N/m to 4×10^6 N/m. A low equivalent stiffness is one reason why the rotor will not recover from a strong base shock. Thus, the rotor should have an appropriate equivalent support stiffness to avoid the destructive backward dry whirl and dry whip.

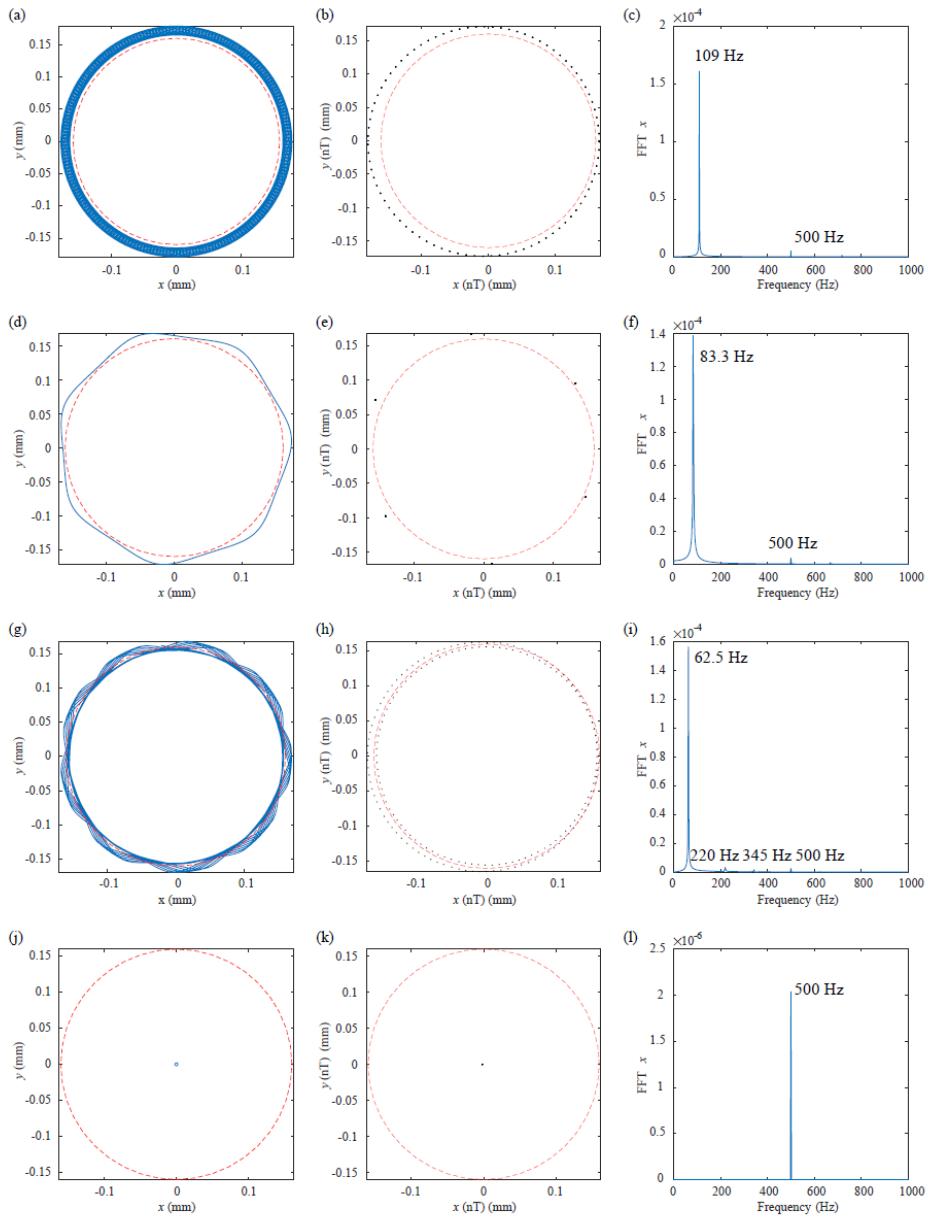

Figure 14: Dynamic analysis for the equivalent stiffness, k_e. (a)(b)(c): rotor trajectory, Poincaré map and frequency spectrum for $k_e = 2\times10^5$ N/m; (d)(e)(f): rotor trajectory, Poincaré map and frequency spectrum for $k_e = 5.024\times10^5$ N/m; (g)(h)(i): rotor trajectory, Poincaré map and frequency spectrum for $k_e = 1.15\times10^6$ N/m; (j)(k)(l): rotor trajectory, Poincaré map and frequency spectrum for $k_e = 2\times10^6$ N/m

Figure 15 shows the bifurcation diagrams for equivalent damping ratios in the range $0.001 \le \xi_e \le 0.031$ in the horizontal and vertical directions. The results show that for damping ratios less than $\xi_e = 0.0125$, the system is irregular. As with the equivalent stiffness analysis, quasi-periodic motion is the major motion mode in this parameter range. $4T$ periodic motion can be observed for $\xi_e = 0.003533$ since the rotor rotational frequency of 500 Hz is four times the backward dry whirl frequency of 125 Hz. The multiple frequencies and their superposition only appear in the range of

$\xi_e = 0.0105 - 0.0125$.

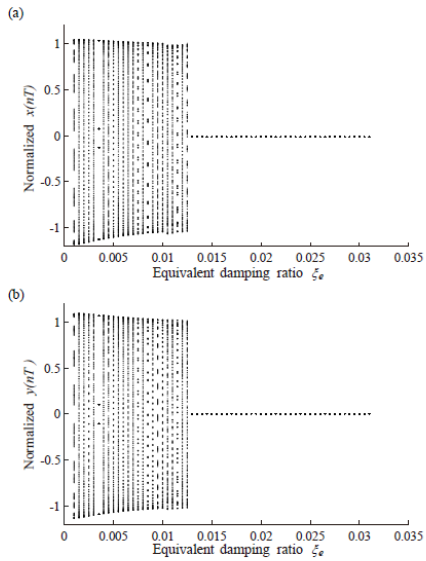

Figure 15: Bifurcation diagrams of the equivalent damping ratio, ξ_e: (a) x(nT), (b) y(nT), (a_1 = 10 G, w = 500 Hz(30000 rpm), r_0 = 0.15 mm, $k_e = 1 \times 10^6$ N/m, $e = 2 \times 10^{-6}$ m)

For damping ratios greater than $\xi_e = 0.0125$, the rotor motion is periodic in the horizontal and vertical directions. Similar to the results of Fig. 7, the system only experiences a very fast rebound and then recovers progressively.

In addition, the analysis indicates that the rotor backward dry whirl frequency decreases from 157.5 Hz to 55 Hz as the equivalent damping ratio increases from 0.001 to 0.031. Thus, small equivalent damping ratio can also be one of the reasons why the rotor cannot recover from strong base shocks. The equivalent damping ratio of the controller should also be designed appropriately to avoid the backward dry whirl and dry whip attracting.

4.2.4 Effect of initial position

Previous research on the rotor dynamics during a drop down event [46] showed the initial rotor position affected the dynamics. In order to perform parametric analysis more accurately, the rotor position was always the same when base shock occurred in all the above simulations in this study.

The effect of the initial rotor position on the shock response was also investigated numerically. In the simulation, a rotor operating at rated rotational speed of 30,000 rpm was subjected to a 10G base shock with the rotor at different positions. However, the results showed that the rotor dynamics were not affected much by the initial rotor position and the dynamic modes did not change as long as the other system parameters

were unchanged. Thus, the detailed simulation results will not be repeated here.

5. Conclusions

The nonlinear dynamics of a rotor-AMB-TDB system were studied with strong base shocks while the AMBs were still operating. The governing equations were solved numerically due to nonlinear effects of the contact forces to study the system dynamics. Dynamic trajectory, FFT and STFT spectra, Poincaré maps, and bifurcation diagrams were used to identify the dynamic behavior for various operating parameters.

The results indicate that base shock can trigger complex nonlinear dynamics with periodic, *KT*-periodic, quasi-periodic motion or jump phenomenon. The evolution of the rotor after a base shock can be categorized into three motion modes. The dry friction tangential forces are responsible for the backward whip/whirl contact modes, and the large residual unbalanced mass can cause continuous rebounds.

The parametric analysis showed that various values of the radial clearance can lead to *KT*-periodic or quasi-periodic motion for $r_0 \le 0.2\ \mathrm{mm}(\bar{\mathrm{r}} \le 1\%)$, with periodic motion for r_0 greater than 0.2 mm. The unbalance eccentricity can lead to *KT*-periodic, quasi-periodic motion, or jump phenomenon for $e \ge 3.6\times10^{-6}$ m, with periodic motion when the unbalance eccentricity is less than 3.6×10^{-6} m. Variations of the equivalent stiffness will lead to *KT*-periodic or quasi-periodic motion for $1\times10^{5}\ \mathrm{N/m} \le \mathrm{k_e} \le 1.25\times10^{6}$ N/m, with periodic motion for $k_e > 1.25\times10^{6}$ N/m. Variations of the equivalent damping will lead to *KT*-periodic or quasi-periodic motion for $0.001 \le \xi_e \le 0.0125$, with periodic motion for $\xi_e > 0.0125$. In addition, octave responses and frequency superposition are often observed. The initial rotor position and rotor velocity have little effect on the shock response.

Continuous dry whirl, whip and rebounds will lead to large contact loads, which are expected to affect the TDB lifetime. The parametric analysis in this paper has a major effect on the rotor-AMB-TDB system. Therefore, the system design parameters should have reasonable values so that the rotor does not experience these undesirable effects when subjected to base shock.

Acknowledgments

This work was supported by the National Key R & D Program of China (Grant No.2018YFB2000100). The authors acknowledge thank Professor David M. Christopher from Tsinghua University for revising the English.